

# Gamma-Neutron Activation Experiments using Laser Wakefield Accelerators\*

W.P. Leemans, D. Rodgers, P.E. Catravas, C.G.R. Geddes, G. Fubiani, E. Esarey,

B.A. Shadwick, R. Donahue, and A. Smith

*Ernest Orlando Lawrence Berkeley National Laboratory*

*University of California, Berkeley CA 94720*

## Abstract

Gamma-neutron activation experiments have been performed with relativistic electron beams produced by a laser wakefield accelerator. The electron beams were produced by tightly focusing (spot diameter  $\approx 6 \mu m$ ) a high power (up to 10 TW), ultra-short ( $\geq 50$  fs) laser beam from a high repetition rate (10 Hz) Ti:sapphire ( $0.8 \mu m$ ) laser system, onto a high density ( $> 10^{19} \text{ cm}^{-3}$ ) pulsed gasjet of length  $\approx 1.5$  mm. Nuclear activation measurements in lead and copper targets indicate the production of electrons with energy in excess of 25 MeV. This result was confirmed by electron distribution measurements using a bending magnet spectrometer. Measured  $\gamma$ -ray and neutron yields are also found to be in reasonable agreement with simulations using a Monte-Carlo transport code.

PACS numbers: 52.75.Di, 52.40.Nk, 41.75.Jv, 41.75.Ht

---

\*Work supported by Department of Energy under Contract No.DE-AC-03-76SF0098.

## I. INTRODUCTION

Acceleration of electrons to energies as high as 100 MeV over mm-size distances using laser wakefield acceleration, has been demonstrated in several experiments [1–7].

These energy gains correspond to accelerating electric fields in plasmas greater than 30 GV/m. The excitation of these large amplitude plasma waves was done by operating in the self-modulated laser wakefield acceleration regime (SM-LWFA) [8–10]. In this regime a single, long laser pulse with duration  $L > \lambda_p$  breaks up into a train of short pulses, each of which has a width on the order of the plasma wavelength  $\lambda_p$ . Associated with the break up of the long pulse and the formation of the pulse train is a large amplitude plasma wakefield. The fields of this wave are sufficiently large to self-trap electrons from the background plasma, and accelerate them to high energies ( $\approx 100$  MeV). In addition to the pulse length criterion, the pulse power  $P$  should exceed the critical power  $P_c = 17\omega^2/\omega_p^2$  GW. Since  $\lambda_p \sim n_0^{-1/2}$  and  $P_c \sim n_0^{-1}$ , for fixed laser parameters, the conditions  $L > \lambda_p$  and  $P > P_c$  can usually be satisfied by operating a sufficiently high plasma density.

In this paper we present the first measurement of nuclear activation in lead and copper targets using electron beams produced by a SM-LWFA. Using the short pulse, high peak power and high repetition rate Ti:Al<sub>2</sub>O<sub>3</sub> laser system at the l’OASIS laboratory at Lawrence Berkeley National Laboratory (LBNL), relativistic electron bunches with sufficiently high charge per bunch were produced to generate radio-isotopes in the target material, from which an unambiguous determination can be made that high energy electrons were indeed generated. In addition, on-line detection of neutron and gamma radiation was used to optimize the performance of the laser driven accelerator. Details of the experiment are presented followed by comparison of the activation results with simulations.

## II. TARGET DESIGN

A  $\gamma, n$  activation scenario was chosen to provide information on a lower bound to the electron beam maximum energy. The basic principle is to stop the electron beam in an appropriate target and use the Bremsstrahlung  $\gamma$ -rays to activate the target material. The reaction products are then analyzed by  $\gamma$ -spectroscopy for identification. The various reactions,  $(\gamma, n)$ ,  $(\gamma, 2n)$ , and  $(\gamma, 3n)$ , have  $\gamma$ -ray threshold energies that must be exceeded in order for the reaction to occur. These thresholds generally increase by 10-15 MeV per neutron released in a given reaction.

There are two possible implementations of this method: on-line  $\gamma$ -ray spectroscopy simultaneous with the electron beam generation, or production of longer-life decay products followed by off-line spectroscopy in a  $\gamma$ -ray spectroscopy facility. The primary advantage of the first implementation is that it allows detection of very short-life ( $<5$ -minute) decay products, in addition to the longer-life products. However, this method requires a high efficiency, portable germanium detector and very close coupling between target and detector to provide maximum counting efficiency. Furthermore it suffers from interferences from the prompt Bremsstrahlung and shower  $\gamma$ -rays. For these reasons, the target in these experiments was designed to optimize production of longer-life products permitting use of the off-line counting method.

The target material was designed to maximize the high energy Bremsstrahlung yield, generate reaction products with half-life time greater than 5 minutes (but shorter than 2 days) that emit detectable quantities of characteristic  $\gamma$ -rays, provide incremental indicators over a  $\gamma$ -ray energy range from 8 MeV to 30 MeV, and be practical to use (available and inexpensive). Candidate elements and reaction products are listed in Table I which has used Ref. [11] as a source of nuclear data.

For each reaction product, a detectability index was calculated given by the product of the natural isotopic abundance times the  $\gamma$ -ray abundance (fraction of nuclear disintegrations that produce the specific  $\gamma$ -ray) divided by the product of the  $\gamma$ -ray energy times the half

life. The higher this index, the easier it is to detect the product for a given number of nuclei generated. Almost all the products emit 511 keV annihilation  $\gamma$ -rays from positron emission, which are not shown in the table. Since this peak is so common, it cannot be used to identify isotopes except by half-life decay studies, and therefore was ignored when determining detectability.

The target used in the experiments consisted of 13 two-piece blocks of various sizes, each with 6.3 mm of Pb at the front and 12.7 mm of Cu at the back. The Cu was selected, because it had three reactions  $[(\gamma, 1n), (\gamma, 2n), (\gamma, 3n)]$  detectable with a  $\gamma$ -ray energy spread of 10.8 MeV to 31.4 MeV. Figure 1 shows the cross section for  $(\gamma, n)$  and  $(\gamma, 2n)$  reactions in Cu<sup>63</sup>. Pb was chosen to generate Bremsstrahlung photons as well as for the complimentary  $(\gamma, n)$  indicators at 8 and 15 MeV. The choice of thickness of the Pb was a compromise between maximum yield of high energy Bremsstrahlung photons, and minimal absorption before entering the Cu. The blocks were glued with cyano-acrylate to an aluminum backing plate in a bulls eye pattern around a central target. The central target segment was constructed as a circular piece 25.4 mm diameter to be placed in the center of the beam axis. Twelve off-axis segments were produced from 12.7 mm x 50 mm rectangular pieces. The radius of the inner (outer) ring was 3.8 (7.6) cm, corresponding to an angle between the laser beam and ring of 76 (138) mrad. The target assembly was placed in the vacuum chamber between the pellicle mirror and the Be exit window, approximately 50 cm from the gasjet.

### III. EXPERIMENTAL SET-UP AND RESULTS

The lay-out of the experiment is shown in Fig. 2. The high power laser beam was produced with a Ti:Al<sub>2</sub>O<sub>3</sub> laser which is described in Ref. [12,13]. Pulses from a Kerr lens modelocked Ti:Al<sub>2</sub>O<sub>3</sub> oscillator, lasing at about  $\lambda = 0.8 \mu m$  were first stretched by a grating stretcher with all-reflective optics, to a length of up to 300 ps, controllable through the bandwidth of the injected oscillator pulses. The stretched pulses were amplified in a regenerative amplifier, pumped with a 1 kHz intra-cavity doubled Nd:YLF laser. The output

of the regenerative amplifier, 1.0 - 1.2 mJ per pulse, was sent to a three-pass pre-amplifier, producing about 40 mJ per pulse at a repetition rate of 10 Hz. A fraction of the pulse (8%) was split off and sent to a large aperture five pass main amplifier (AMP1). After five passes in AMP1, an energy level of up to 1 J per pulse was reached, equivalent to an average power of 10 W. This high energy 200-300 ps chirped pulse was propagated into a shielded cave below the laser lab through an evacuated beam pipe and compressed in a vacuum compressor to peak powers of 8-10 TW in a pulse as short as 50 fs. Vacuum is required at these power levels to minimize linear and non-linear dispersion effects. This high power pulse served as the main drive laser pulse for the self-modulated LWFA experiment.

The laser pulse duration and, consequently, amount and sign of the laser wavelength chirp, was varied by changing the grating distance in the vacuum compressor. Measurement of the laser pulse duration and laser chirp was done with a commercial single shot autocorrelator (SSA) and a frequency resolved optical gating (FROG) system, respectively. Both systems are located outside the vacuum chamber. After compression, the laser beam was reflected with mirror M1 onto an F/4, 30 cm focal length off-axis parabola (OAP), which focused the beam onto a high pressure pulsed gasjet. The gasjet was operated with H<sub>2</sub>, He and N<sub>2</sub> at backing pressures up to 72 bar. The OAP alignment was optimized for minimum aberrations, providing a spot size of approximately  $w = 6\mu\text{m}$ , or Rayleigh length  $z_R = \pi w^2/\lambda = 141\mu\text{m}$ . A final steering mirror after the OAP was used to provide independent control of the pointing direction. After the interaction region, the main laser beam was reflected by a gold or silver coated, 2  $\mu\text{m}$  thick nitrocellulose pellicle. This material and thickness was chosen to minimize Coulomb scattering of electrons propagating through it, while still maintaining optical flatness. After appropriate attenuation, the spectral properties and pulse duration of the exiting laser beam were then analyzed on either a FROG system or an imaging spectrometer.

The density profile of laser produced plasma was measured using side-on interferometry with a single femtosecond laser pulse. The interferometer was of the folded-wave type. Laser beam radiation leaking through M1 was reflected onto a variable optical delay line and sent

orthogonally to the main laser beam through the interaction region above the gasjet. After exiting the chamber the probe beam was split and recombined, providing equal pathlengths for both beams to a CCD camera. The interaction region was imaged onto the camera using an achromatic lens. Phase changes imparted by the plasma to the laser beam were extracted from the interferograms using a fringe tracing program. Density profiles were obtained by Abel inverting the two dimensional phase profiles. A typical measured profile is shown in Fig. 3. Plasma densities on the order of  $n_e = 1 - 3 \times 10^{19} \text{ cm}^{-3}$  were produced, corresponding to plasma wavelengths  $\lambda_p$  and dephasing distances  $L_d = \lambda_p^3/\lambda^2$  on the order of  $10.6 - 6.1 \mu\text{m}$  and  $1.84 - 0.35 \text{ mm}$ , respectively.

The peak power of the laser was varied using both the pulse duration and laser energy. For the results discussed here the laser peak power was tuned to about 8.3 TW. The critical power ranged from 2.9 to 1 TW for the density range used in the experiment, and hence was exceeded for all data shown in this paper. The cold non-relativistic wavebreaking amplitude of the plasma wave was  $E_{WB} = cm_e\omega_p/e \approx 304 - 520 \text{ GV/m}$ .

The total charge per bunch of the electron beam was measured using a commercial integrating current transformer (ICT). The spatial profile was measured with a phosphor screen that was imaged onto a 16 bit charge coupled device (CCD) camera. The energy distribution of the electron beam was measured by placing the same detector downstream of a dipole spectrometer magnet. The ICT, as well as an identical magnetic dipole had been previously calibrated against a Faraday cup and used at the Beam Test Facility, located at the Advanced Light Source of LBNL, with 30 ps long bunches at 50 MeV containing typically 1-1.5 nC.

Neutron and gamma rays produced during operation of the experiment were monitored with a variety of detectors, allowing both use of this radiation as a beam diagnostic and for the evaluation of various detector performances. The  $\gamma$ -radiation was Bremsstrahlung from the deceleration of the electron beam in the target and other chamber material, while neutrons were produced by interactions of high energy  $\gamma$ -rays with the target and chamber material. The short duration of these  $\gamma$ -ray bursts precludes measurement of electron beam

energy through on-line  $\gamma$ -ray spectroscopy as this requires single photon detection, with delays between detection events on the order of a  $\mu$ s. Neutron production, however, requires production of  $\gamma$ -rays with energy in excess of at least 8.4 MeV and therefore can serve as a rough diagnostic of high energy electron production.

A Health Physics Instruments (HPI) Model 6020 Geiger-Mueller (GM) area  $\gamma$ -ray monitor operating in pulse counting mode was placed outside the vacuum chamber near the target. Gamma-ray bursts from the beam could be picosecond or even sub-picosecond in duration, much shorter than the resolving time of a GM detector which is on the order of ten's of milliseconds. Therefore, the response was limited to a maximum of one count per beam pulse, regardless of true dose. With a pulse rate of 5 Hz, this results in a maximum reading of 0.6 mR/hr dose equivalent. This detector was therefore used primarily as a high sensitivity indicator for the onset of  $\gamma$ -ray production.

Two ion chamber based radiation monitors were placed near the vacuum chamber and near the electron beam dump (1.5 m downstream from the gasjet) to provide a quantitative measurement of the  $\gamma$ -ray yield per bunch at 90° and in the forward direction, respectively.

To provide a measure of total integrated  $\gamma$ -ray dose, a Victoreen Model 450P pressurized ion chamber survey meter was placed on top of the vacuum chamber. During a typical run time of 6 hours, a dose in excess of 2 R was recorded.

Neutron monitoring relied on two different types of detectors. The first was an HPI 6060 He3 detector with an Anderson-Braun (A-B) type moderator with pulse output. Accurate response of this detector with very short pulses is possible because of the moderation time of the A-B moderator, which delays and spreads the arrival time of the incident neutrons over a period of milliseconds, well within the approximately 1  $\mu$ sec resolving time of the detector. The second neutron detector was an HPI 2080 neutron area monitor. The 2080 uses a Ag-wrapped GM tube for primary neutron detection and a Sn-wrapped GM tube in anti-coincidence for  $\gamma$ -ray response suppression. The detection process uses a large polyethylene moderator to thermalize the neutrons and the (n, $\gamma$ ) reaction on  $^{109}\text{Ag}$  to produce 24.6 s half life  $^{110}\text{Ag}$ , which is then detected by the GM detector. This type of detector can detect

very short radiation pulses because the half life of the  $^{110}\text{Ag}$  acts to delay and broaden the response, in addition to the moderation time effect.

To ensure that the signal detected on the  $^3\text{He}$  neutron detector was indeed due to neutrons with minimal contribution from the high  $\gamma$ -ray radiation levels, a comparison was performed between a  $^3\text{He}$  detector with a A-B moderator located behind a 20 cm thick lead shield, and two neutron  $\text{He3}$  detectors which were not shielded, one with an A-B moderator and one with a Cd-liner. The detector with the Cd sleeve should respond only to  $\gamma$ -radiation, since the  $^3\text{He}$  detectors are sensitive only to thermal neutrons which the Cd absorbs. The neutron yield obtained from the lead shielded neutron detector and the  $\gamma$ -ray corrected unshielded, but moderated neutron detector, were in excellent agreement.

#### **A. Electron, neutron and $\gamma$ -ray correlations.**

In Fig. 4, electron, neutron and  $\gamma$ -ray yield (measured near the target) versus position of the gasjet is shown. Here the zero position refers to the vacuum laser focus position coinciding with the center of the gasjet. In general, the different yields were found to be very well correlated with each other and large increases in yield were observed by adjusting the position of the gasjet front edge with respect to the location of the vacuum focus. The neutron yield was found to increase with forward directed  $\gamma$ -ray yield, consistent with the production of higher energy, more collimated electrons (see Fig. 5). As can be seen in Fig. 4, electron, neutron and  $\gamma$ -ray yields peaked for a gas jet position around  $-1.4$  mm. In this position the laser beam is focused on the front edge, providing for the longest interaction distance between the high intensity laser pulse and the gasjet. This in turn can result in the longest acceleration distance and hence highest energy gain for trapped electrons. Also, due to the parabolic density profile of the gasjet, dephasing length of the electrons may be increased due to plasma waves moving up a density gradient.

A second maximum for the electron yield was obtained for a gasjet position around  $-0.8$  mm. However, neutron and  $\gamma$ -ray yield near the target were considerably lower indicating



that electrons produced at this gasjet position have lower energy. We hypothesize that, for laser pulses focused into the gasjet plume, ionization induced refraction effects [14,15] could prevent the laser pulse from reaching the vacuum spot size leading to a reduced peak intensity and hence lower amplitude of the excited laser wakefield. In addition, the net interaction distance could be reduced due to the fact that less plasma is ahead of the laser pulse when it is focused inside the jet, leading to a further reduction of the net energy gain.

The yield in electrons and neutrons was also found to scale with increased laser power (see Fig. 6). The minimum power at which neutrons were observed was on the order of 2.8 TW, which is comparable to the critical power for  $n_e = 10^{19}\text{cm}^{-3}$ . In addition, the neutron yield was found to be dependent on laser chirp: significantly larger yields were obtained for positively chirped laser pulses (red wavelengths in the front of the pulse, blue in the back). Several possible mechanisms are being investigated at the present time and will be reported in a separate paper.

## B. Gamma-ray Analysis of the Target

After approximately 3 hours of target activation, the target plate was removed from the vacuum chamber, transferred to the remote counting facility and individual blocks were removed from the plate. Three intrinsic Germanium  $\gamma$ -ray spectrometers were used for counting, with the firsts counts beginning within 15-minutes of the beam-off time. Most of the counting used a 115% relative efficiency n-type detector with a magnesium endcap. Other detectors used were an 80% and a 30% relative efficiency p-type detectors, both with aluminum endcaps. The detectors were located at a dedicated ultra-low background counting facility at LBNL. All spectra were accumulated over 16384 channels over the energy range of 30 to 3500 keV.

The vast majority of activity seen in the first minutes of counting was at a  $\gamma$ -ray energy of 511 keV, as expected. The central target segment was counted on the 115% detector. Eight 2-minute long counts were taken, which were followed by five 10-minute counts, with

the intent of deriving half-life information from the decay of the 511 keV peak. The decay followed a 10-minute half-life at first, indicating that significant  $^{62}\text{Cu}$  was in the sample, produced from a  $(\gamma, n)$  reaction on  $^{63}\text{Cu}$ , which has a 10.8 MeV threshold. The activity vs. time for an 80 minute period is shown in Fig. 7. Longer counts were then taken to maximize detection of low activity gamma rays.

The off-axis segments were counted on the other two detectors. The inner ring of four were counted individually. Due to time constraints, the outer ring of eight was divided into two groups of 4 each and each group counted as a single sample. The distribution of relative activity from the 511 keV peak on the target, as shown in Fig. 8, is indicative of a well collimated relativistic electron beam emerging from the gasjet. The asymmetry arises from the fact that (a) the electron beam was not perfectly incident on the middle of the target and (b) the frame of the mount in which the pellicle mirror was held partially shielded the left hand side of the target.

We identified  $\gamma$ -rays for all the target reactions except the  $^{63}\text{Cu}(\gamma, 3n)$  to  $^{60}\text{Cu}$  reaction. The  $\gamma$ -ray analysis results are shown in Table II. From the initial 511-keV decay, we resolved the 9.7-minute half-life of the  $^{62}\text{Cu}$  from the  $^{63}\text{Cu}(\gamma, n)$  reaction (10.8 MeV threshold) and used this to derive the  $^{62}\text{Cu}$  activity at the end of the run. Although the 1345 keV photopeak of the  $^{64}\text{Cu}$  from the  $^{65}\text{Cu}(\gamma, n)$  reaction (9.9 MeV threshold) was observed, better sensitivity was obtained by using the 511-keV annihilation peak and establishing the  $^{64}\text{Cu}$  half-life for the calculation (counted after sufficient time had elapsed for the 9.7 minute  $^{62}\text{Cu}$  to decay completely). We used the 656 keV photopeak to quantify the 3.3 hour half-life of  $^{61}\text{Cu}$  produced by the  $^{63}\text{Cu}(\gamma, 2n)$  reaction (19.7 MeV threshold). We quantified the  $^{203}\text{Pb}$  from the  $^{204}\text{Pb}(\gamma, n)$  reaction (8.4 MeV threshold) from the 269 keV, as anticipated. A 373 keV  $^{61}\text{Cu}$  peak interfered with the 374 keV  $^{204m}\text{Pb}$  peak and therefore we used the higher energy 899 keV photopeak for the  $^{204m}\text{Pb}$  analysis.

For each product nuclide, we calculated the activity in counts per minute, decay corrected to the end of the run, then divided by the  $\gamma$ -ray abundance and detector efficiency to yield the disintegrations per minute at the end of the run. Steady production results in an

equilibrium disintegration rate after a large number of half lives. The disintegration rate  $A$  as a function of time is given by  $A = P(1 - e^{-\kappa t})$  where  $A$  is in disintegrations/minute,  $P$  is the production rate in atoms/minute,  $\kappa$  is the decay constant in units of  $\text{min}^{-1}$  and  $t$  is the elapsed time after the onset of production. For each reaction product,  $P$  was obtained from  $P = A/(1 - e^{-\kappa t})$ , where  $A$  equals the calculated dpm-count at the end of the run. The total number of atoms created of each reaction product was obtained by multiplying  $P$  with an effective run time, roughly equal to 210 minutes.

As an aid in comparing the results for the various reactions, we normalized the number of atoms created for each reaction to 100% natural isotopic abundance of the applicable target isotope, as shown in the final column of the table. These calculations show that the  $^{65}\text{Cu}(\gamma, n)$  and  $^{63}\text{Cu}(\gamma, n)$  reactions occurred at very similar normalized rates, which was expected since they have similar reaction thresholds and cross sections. Successful observation of the 3.3 hr half-life time of  $^{61}\text{Cu}$  from the  $^{63}\text{Cu}(\gamma, 2n)$  reaction confirmed that a significant fraction of the  $\gamma$ -ray flux, and hence electron beam, had an energy above the 19.7 MeV threshold for this reaction. Observation of the  $^{204}\text{Pb}(\gamma, n)$  and  $^{206}\text{Pb}(\gamma, 2n)$  reactions supported qualitatively the reactions observed in the Cu target, but we could not derive any quantitative conclusions due to lack of references for the cross sections. Even estimates of the relative cross sections of these two reactions proved difficult because the  $^{204m}\text{Pb}$  from the  $^{206}\text{Pb}(\gamma, 2n)$  reaction probably competes with  $^{204}\text{Pb}$ , which is essentially stable. This competition may explain why the observed  $^{204}\text{Pb}(\gamma, n)$  normalized reaction rate was almost 1000 times higher than that of the  $^{206}\text{Pb}(\gamma, 2n)$  rate. We observed no indication of the 24 minute half-life of  $^{60}\text{Cu}$ , produced by the  $^{63}\text{Cu}(\gamma, 3n)$  reaction (31.4 MeV threshold). A limiting value was estimated using three standard deviations of the gross counts in the 1332 keV region of the spectra of the first 26 minutes of counting. This resulted in a limiting value of 59 dpm at the end of the run or a normalized atom yield of  $< 1.8 \times 10^4$ .

#### IV. SIMULATION RESULTS

Calculations were made to estimate the production of  $^{62}\text{Cu}$  ( $T_{1/2} = 9.7$  min) via the  $^{63}\text{Cu}(\gamma, n)$  reaction in the Cu target. Monte Carlo calculations were performed with the MCNP code [16]. In the simulations, a pencil-like e-beam was incident on a target consisting of 1/4" of Pb followed by 1/2" of Cu, both 1" in diameter. The incident e-beam energy distribution for the simulations was obtained from measurements using the bending magnet spectrometer. The distribution was obtained as follows. The light yield from the electron beam incident on the phosphor screen was measured for different current settings. After deconvolution of the electron beam spot size for zero magnetic field, and differentiation, the resulting curve was fitted using  $f(p) = 3.57 \times 10^7 e^{[-0.3p+4.9]}$  ( $e^-/\text{pulse}$ ) where  $p$  is the  $e^-$  momentum in [MeV/c]. It was assumed that the light yield from the phosphor was independent of incident electron energy and linear with amount of charge. The latter assumption had been verified for electrons at 50 MeV.

The measured  $e^-$  momentum distribution was converted to kinetic energy and sampled in MCNP from 0 to 100 MeV. Flat energy biasing was used to ensure a statistically significant sampling of high energy  $e^-$ 's. Particles were sampled with a frequency determined by an assigned bias level but with a weight that is inversely proportional to that level. This type of biasing of the sampling in MCNP preserves the original distribution but reduces statistical uncertainty in energy regions of greater importance that may be undersampled in a non-biased approach. In addition, high-energy Bremsstrahlung yield was also biased in a similar manner to reduce uncertainty of the photon flux in the 12-25 MeV energy range of the  $^{63}\text{Cu}(\gamma, n)$  reaction.

The photon flux integrated over the entire Cu cell was calculated as a function of photon energy. MCNP does not simulate photonuclear reactions, therefore the  $^{63}\text{Cu}(\gamma, n)$  cross section [17] as a function of energy was provided as input to MCNP under the form of a response function to be folded into the Cu cell flux.

The activity  $A$  of  $^{62}\text{Cu}$  is then estimated as:  $A = \lambda N = \int dE \sigma(E) \phi(E) N_t (1 - e^{-\lambda T})$

where  $\sigma(E)$  is the  $^{63}\text{Cu}(\gamma, n)$  cross section as a function of energy,  $\phi(E)$  is the photon flux in the Cu as a function of energy,  $N_t$  is the number of  $^{63}\text{Cu}$  target atoms,  $\lambda$  is the  $^{62}\text{Cu}$  decay constant and  $T$  is the irradiation time. In this manner a  $^{62}\text{Cu}$  saturation activity of  $2.12 \mu\text{Ci}$  was estimated. This is a factor of 10x higher than the measured value of  $0.29 \mu\text{Ci}$ . However, the simulation of the  $^{62}\text{Cu}$  activation was performed under the assumption that the entire beam hit the 1" diameter central target. In the experiment, significant activity was also measured in the outer target segments. Taking the observed activation per area ( $\mu\text{Ci}/\text{cm}^2$ ) of the inner and outer rings to be representative of a solid circular target extending from the central target to a 2" radius, and from the inner ring to a radius of 3", respectively, we obtain a total equilibrium activity of  $2.5 \mu\text{Ci}$ . This compares well to the simulated value of  $2.12 \mu\text{Ci}$ .

The  $\gamma$ -dose rate at  $90^\circ$  was also estimated by calculating the photon flux at 30 cm and folding in the American National Standards Institute (ANSI) flux-to-dose conversion factors [18]. The target geometry was surrounded by an Al sphere 1" thick, to model shielding effects of the Al vacuum chamber housing the gas jet assembly. The  $\gamma$ -dose rate was estimated to be about 2.2 rad/hr. The result from this simple model is in reasonable agreement with the reading from an integrating ion chamber that gave approximately 2 rad over a 3 hr period.

## V. CONCLUSION

Relativistic electron beams containing on the order of 4-5 nC/bunch, produced in the SM-LWFA regime using a 10 Hz, 10 TW, Ti:Al<sub>2</sub>O<sub>3</sub> laser system, have been used for nuclear activation experiments in composite Pb/Cu targets. The electron beams were generated by focusing this high power laser beam onto a He gasjet. The high charge per bunch and high repetition rate of the experiment enabled radio-isotope production and systematic scanning of various laser and plasma parameters. On-line detection of neutron and  $\gamma$ -ray radiation was used to optimize the performance of the laser driven accelerator. The neutron and forward directed  $\gamma$ -ray yield were found to be well correlated with electron yield, and, as expected,

to depend on laser power and gasjet position. Neutrons were produced for laser pulses with positive chirp that had powers exceeding the critical power for self-focusing. However, much lower neutron yields were obtained for negatively chirped laser pulses. Neutron and  $\gamma$ -ray yield were optimized when the laser beam was focused on the front edge of the gasjet. Through  $\gamma$ -ray spectroscopy and measurement of the 511 keV annihilation photopeak decay rate, several radio-isotopes were identified in the target material, from which an unambiguous determination was made that high energy electrons ( $\geq 25$  MeV) were indeed generated. The production of high energy electrons was independently confirmed using a bending magnet spectrometer. Simulations with the Monte-Carlo based transport code MCNP, using the measured electron distribution, predict activation levels which are in reasonable agreement with the experimental results.

## VI. ACKNOWLEDGMENTS

The authors thank L. Archambault, M. Dickinson, S. DiMaggio, R. Short, G. J. H. Brussaard, J. van Tilborg, K. L. Barat, J. Floyd, E. Wong and T. De Castro for their contributions. We also thank S. Chattopadhyay, J. S. Wurtele and M. van der Wiel for their support. We recently learned about similar nuclear activation measurements performed at Rutherford Appleton Laboratories.

## REFERENCES

- [1] A. Modena, Z. Najmudin, A. E. Dangor, C. E. Clayton, K. A. Marsh, C. Joshi, V. Malka, C. B. Darrow, C. Danson, D. Neely, and F. N. Walsh, *Nature* **377**, 606 (1995).
- [2] K. Nakajima, D. Fisher, T. Kawakubo, H. Nakanishi, A. Ogata, Y. Kato, Y. Kitagawa, R. Kodama, K. Mima, H. Shiraga, K. Suzuki, K. Yamakawa, T. Zhang, Y. Sakawa, T. Shoji, Y. Nishida, N. Yugami, M. Downer, and T. Tajima, *Phys. Rev. Lett.* **74**, 4428 (1995).
- [3] D. Umstadter, S.-Y. Chen, A. Maksimchuk, G. Mourou, and R. Wagner, *Science* **273**, 472 (1996).
- [4] R. Wagner, S. Y. Chen, A. Maksimchuk, and D. Umstadter, *Phys. Rev. Lett.* **78**, 3125 (1997).
- [5] A. Ting, C. I. Moore, K. Krushelnick, C. Manka, E. Esarey, P. Sprangle, R. Hubbard, H. R. Burris, and M. Baine, *Phys. Plasmas* **4**, 1889 (1997).
- [6] C. Moore, A. Ting, K. Krushelnick, E. Esarey, R. F. Hubbard, H. R. Burris, C. Manka, and P. Sprangle, *Phys. Rev. Lett.* **79**, 3909 (1997).
- [7] D. Gordon, K. C. Tzeng, C. E. Clayton, A. E. Dangor, V. Malka, K. A. Marsh, A. Modena, W. B. Mori, P. Muggli, Z. Najmudin, D. Neely, C. Danson, and C. Joshi, *Phys. Rev. Lett.* 2133 (1998).
- [8] P. Sprangle, E. Esarey, J. Krall, and G. Joyce, *Phys. Rev. Lett.* **69**, 2200 (1992).
- [9] E. Esarey, P. Sprangle, J. Krall, and A. Ting, *IEEE Trans. Plasma Sci.* **24**, 252 (1996).
- [10] W. B. Mori, C. D. Decker, D. E. Hinkel, and T. Katsouleas, *Phys. Rev. Lett.* **72**, 1482 (1994).
- [11] R. B. Firestone, V. S. Shirley, C. M. Baglin, S. Y. F. Chu, and J. Zipkin, *Table of Isotopes*, eight ed. (John Wiley and Sons, New York, 1996).

- [12] W. P. Leemans, P. Volfbeyn, K. Z. Guo, S. Chattopadhyay, C. B. Schroeder, B. A. Shadwick, P. B. Lee, and J. S. Wurtele, Phys. Plasmas **5**, 16215 (1998).
- [13] P. Volfbeyn, E. Esarey, and W. Leemans, Phys. Plasmas **6**, 2269 (1999).
- [14] W. P. Leemans, C. E. Clayton, W. B. Mori, K. A. Marsh, A. Dyson, and C. Joshi, Phys. Rev. Lett. **68**, 321 (1992).
- [15] W. P. Leemans, C. E. Clayton, W. B. Mori, K. A. Marsh, P. K. Kaw, A. Dyson, C. Joshi, and J. M. Wallace, Phys. Rev. A **46**, 1091 (1992).
- [16] J. F. Briesmeister, LA-13709-M, Los Alamos National Lab (2000).
- [17] S. C. Fultz, R. L. Bramlett, J. T. Caldwell, and R. R. Harvey, Physical Review B **133**, 1149 (1964).
- [18] American Nuclear Society, *American National Standard Neutron and Gamma-Ray Flux-to-Dose Rate Factors* (ANSI, ANSI/ANS-6.1.1-1977, 1977).



# TABLES

TABLE I. Reactions suitable for delayed counting. The table shows the natural abundance, reaction type, threshold energy of the  $\gamma$ -ray, the half-life time (m=minute, h=hour, d=days), the energy of the characteristic  $\gamma$ -ray emission, its relative abundance, detection index (see above) and the reaction cross-section.

Target	Target	Nat.	React.	Thresh.	Product	T1/2	keV	Abn	Detection	$\sigma$
Element	Isotope	Abn		MeV				%	Index	mbarns
Cu	<sup>65</sup> Cu	31%	$\gamma,1n$	9.9	<sup>64</sup> Cu	12.7 h	1345	0.5	0.01	75
	<sup>63</sup> Cu	69%	$\gamma,1n$	10.8	<sup>62</sup> Cu	9.7m	1172	0.3	0.01	68
	<sup>63</sup> Cu	69%	$\gamma,2n$	19.7	<sup>61</sup> Cu	3.3h	282	12.0	9	12
	<sup>63</sup> Cu	69%	$\gamma,3n$	31.4	Cu60	24m	1332	88	23	n.a.
Pb	<sup>204</sup> Pb	1.4%	$\gamma,1n$	8.4	Pb203	52h	279	81	0.08	n.a.
	<sup>206</sup> Pb	24%	$\gamma,2n$	14.8	<sup>204m</sup> Pb	67m	374	89	57	80
F	<sup>19</sup> F	100%	$\gamma,1n$	10.4	<sup>18</sup> F	110m	511	180	176	11
C	<sup>12</sup> C	98%	$\gamma,1n$	18.7	<sup>11</sup> C	20m	511	180	115	7
Zn	<sup>64</sup> Zn	49%	$\gamma,1n$	11.9	<sup>63</sup> Zn	38m	669	8	4	50
Cr	<sup>50</sup> Cr	4%	$\gamma,1n$	13.0	<sup>49</sup> Cr	42m	153	30	5	30
K	<sup>39</sup> K	93%	$\gamma,1n$	13.1	<sup>38</sup> K	8m	2162	100	6	n.a.
Ni	<sup>58</sup> Ni	68%	$\gamma,1n$	12.0	<sup>57</sup> Ni	36h	1377	82	1	30
	<sup>58</sup> Ni	68%	$\gamma,2n$	22.5	<sup>56</sup> Ni	6d	811	86	0.5	n.a.

TABLE II. Analysis of reaction products where Det. Eff., cpm and dpm stand for detector efficiency, counts and disintegrations per minute, respectively. The gamma abundance (column 4) is from Ref [11].

Target	react.	fract.	$\gamma$	cpm	Det. Eff.	dpm	Equil.	atoms	Norm.
		of equil.	abn.	final	cpm/dpm	final	dpm	prod.	atoms prod.
$^{204}\text{Pb}$	$\gamma, 1n$	0.046	0.810	237	0.109	2,680	58,800	1.23E+07	8.82E+08
$^{65}\text{Cu}$	$\gamma, 1n$	0.174	0.358	1,060	0.055	53,800	310,000	6.50E+07	2.10E+08
$^{63}\text{Cu}$	$\gamma, 1n$	1.000	1.960	70,000	0.055	649,000	649,000	1.36E+08	1.98E+08
$^{206}\text{Pb}$	$\gamma, 2n$	0.885	0.990	10	0.01	971	1,100	2.30E+05	9.6E+05
$^{63}\text{Cu}$	$\gamma, 2n$	0.517	0.108	42	0.045	8,640	16,700	3.51E+06	5.09E+06
$^{63}\text{Cu}$	$\gamma, 3n$	0.998	0.880	< 1.4	0.027	< 58.9	< 59	< 12,400	< 1.80E+04

## FIGURES

FIG. 1. Reaction cross section for  $(\gamma, n)$  and  $(\gamma, 2n)$  in  $^{63}\text{Cu}$  (after ref. [17]).

FIG. 2. Lay-out of experiment showing the laser beam exiting the compressor, being reflected by mirror M1 onto the off-axis parabola (OAP), which focuses it onto the gasjet. The resulting electron beam is measured using the integrated current transformer (ICT) and is dispersed in the magnetic spectrometer onto a phosphor screen. The screen is imaged with the CCD. Plasma densities are measured with the interferometer (INT) and the laser beam is analyzed using the single-shot autocorrelator (SSA), the frequency resolved optical gating system (FROG) and an imaging optical spectrometer (Spec.). The location of the various radiation monitors are indicated.

FIG. 3. Plasma density profile measured with a folded-wave interferometer operating at  $0.8\ \mu\text{m}$ . The gasjet delivering the neutral He gas was operated at 1000 psi reservoir pressure. The parabolic shape indicates that the flow was subsonic. Peak plasma density was on the order of  $2.5 - 3 \times 10^{19}\ \text{cm}^{-3}$ .

FIG. 4. Electron and neutron yield versus gas jet position. The center of the gasjet is at 0 mm. The first peak in electron yield at -1.4 mm, correlates with neutron and  $\gamma$ -ray yield indicating that a significant amount of high energy electrons is produced. The absence of a neutron or  $\gamma$ -ray peak near the second peak in electron yield at -0.7 mm is indicative of lower energy electrons being generated.

FIG. 5. Ratio of forward and  $90^\circ$  directed  $\gamma$ -ray yield, measured with ion chambers, vs. neutron yield showing an increase of neutron yield for an increase in forward peaked  $\gamma$ -ray flux. This correlation is consistent with the fact that neutron production requires generation of a significant high energy component in the electron beam, which is typically produced in a narrower cone than the low energy component.

FIG. 6. Electron and neutron yield versus compressor position. The horizontal axis is the separation between the two final compressor gratings.

FIG. 7. Activity of the 511 keV annihilation photopeak, corrected for  $^{64}\text{Cu}$  contribution, in counts per minute vs. time (solid line) and graph of the expected decay of  $^{62}\text{Cu}$  given its half-life time of 9.7 min (dashed line). The eventual deviation of the two curves indicates the presence of longer lived radio-isotopes.

FIG. 8. Distribution of relative activity on the target. The target consisted of blocks of 6.3 mm thick lead followed by 12.7 mm Cu and was located 50 cm away from the gasjet. The two rings had a radius of 3.8 cm and 7.6 cm, respectively. A relative activity of 1 has been assigned to the 25.4 mm diameter central target. Blocks from the outer ring were counted in two groups of 4, as indicated in the Figure, and had a significantly lower relative induced activity than the central target. The asymmetry arises from the fact that (a) the electron beam was not perfectly incident on the middle of the target and (b) the frame of the mount in which the pellicle mirror was held partially shielded the left hand side of the target.

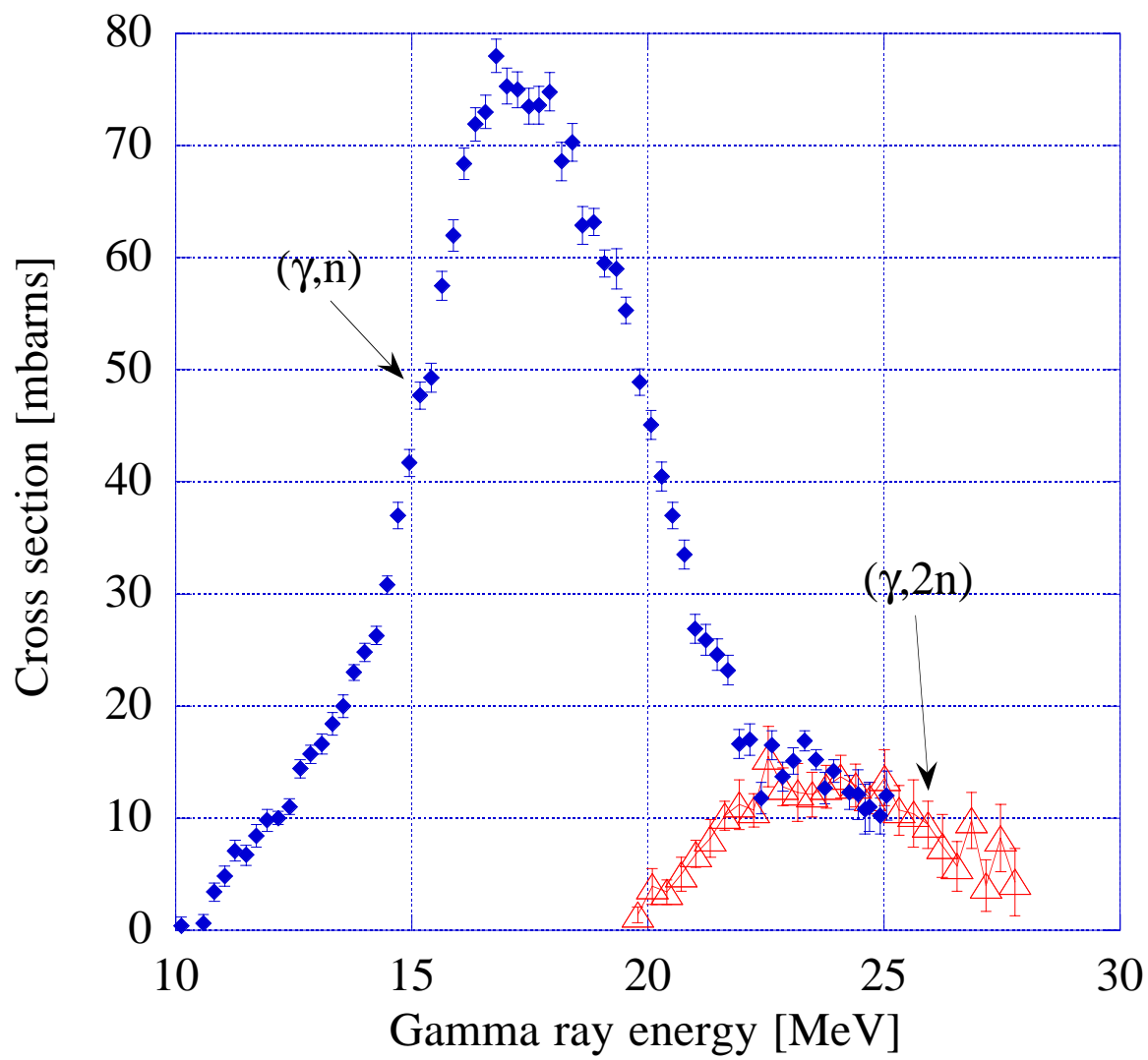


FIG. 1.

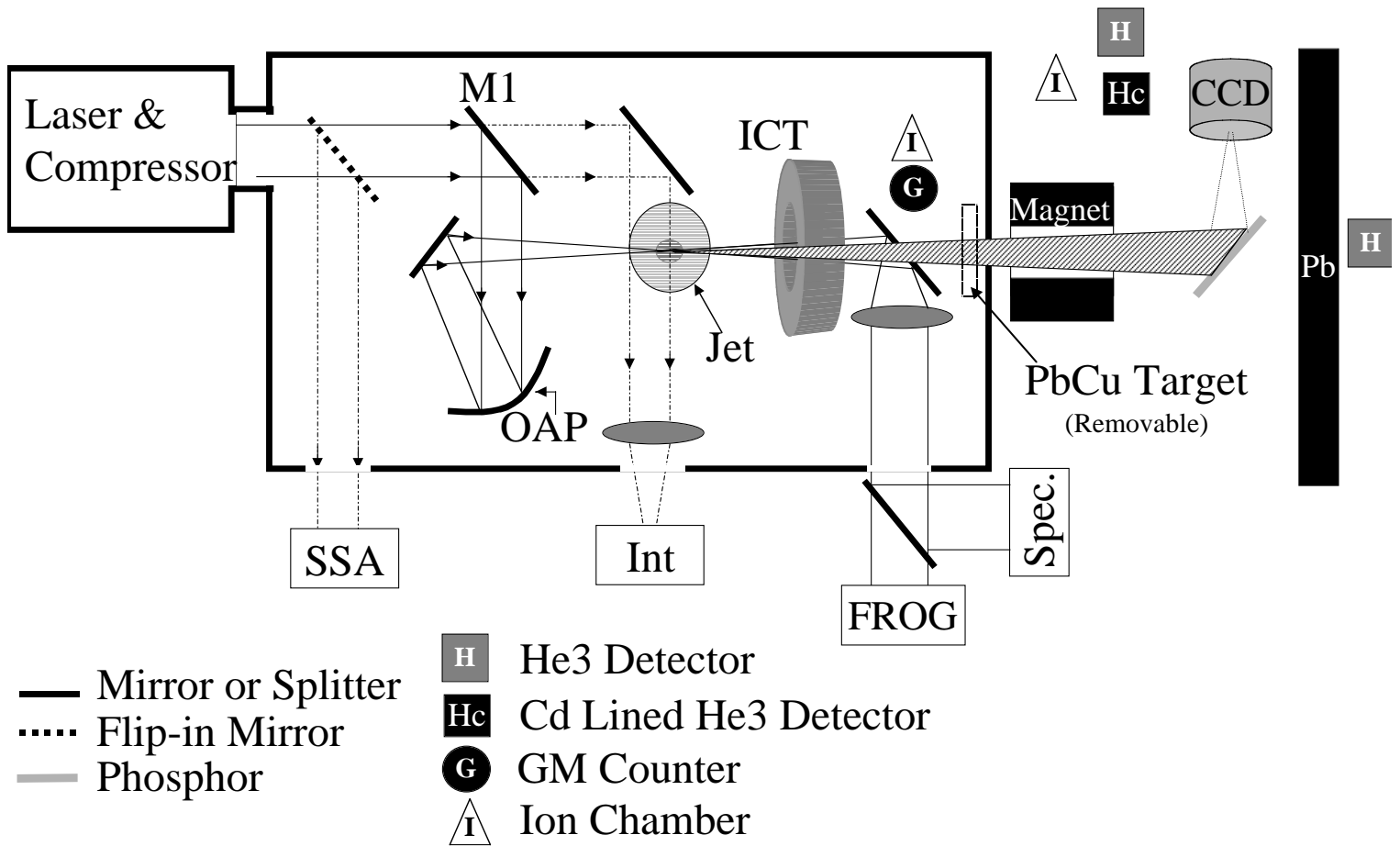


FIG. 2.

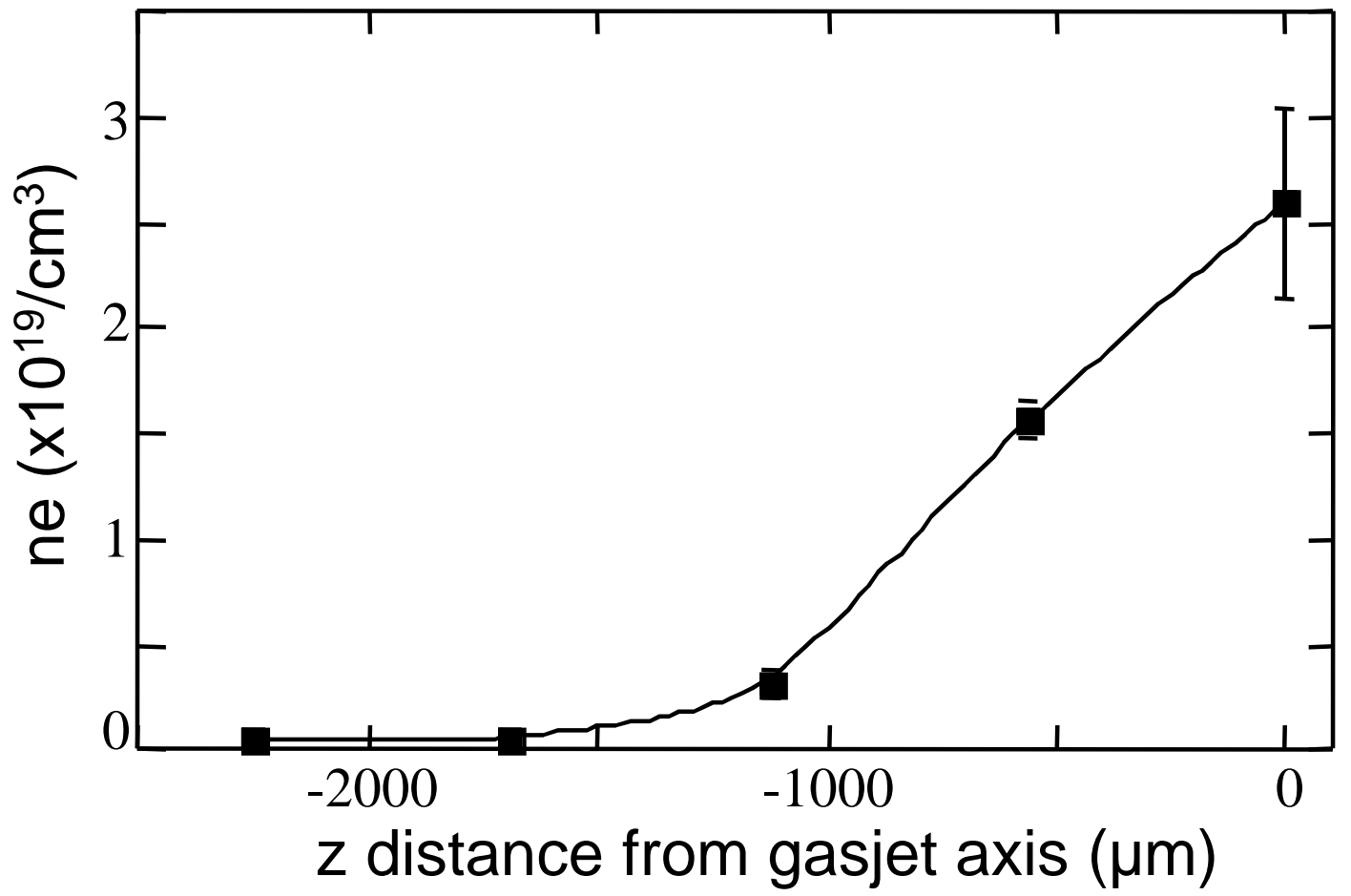


FIG. 3.

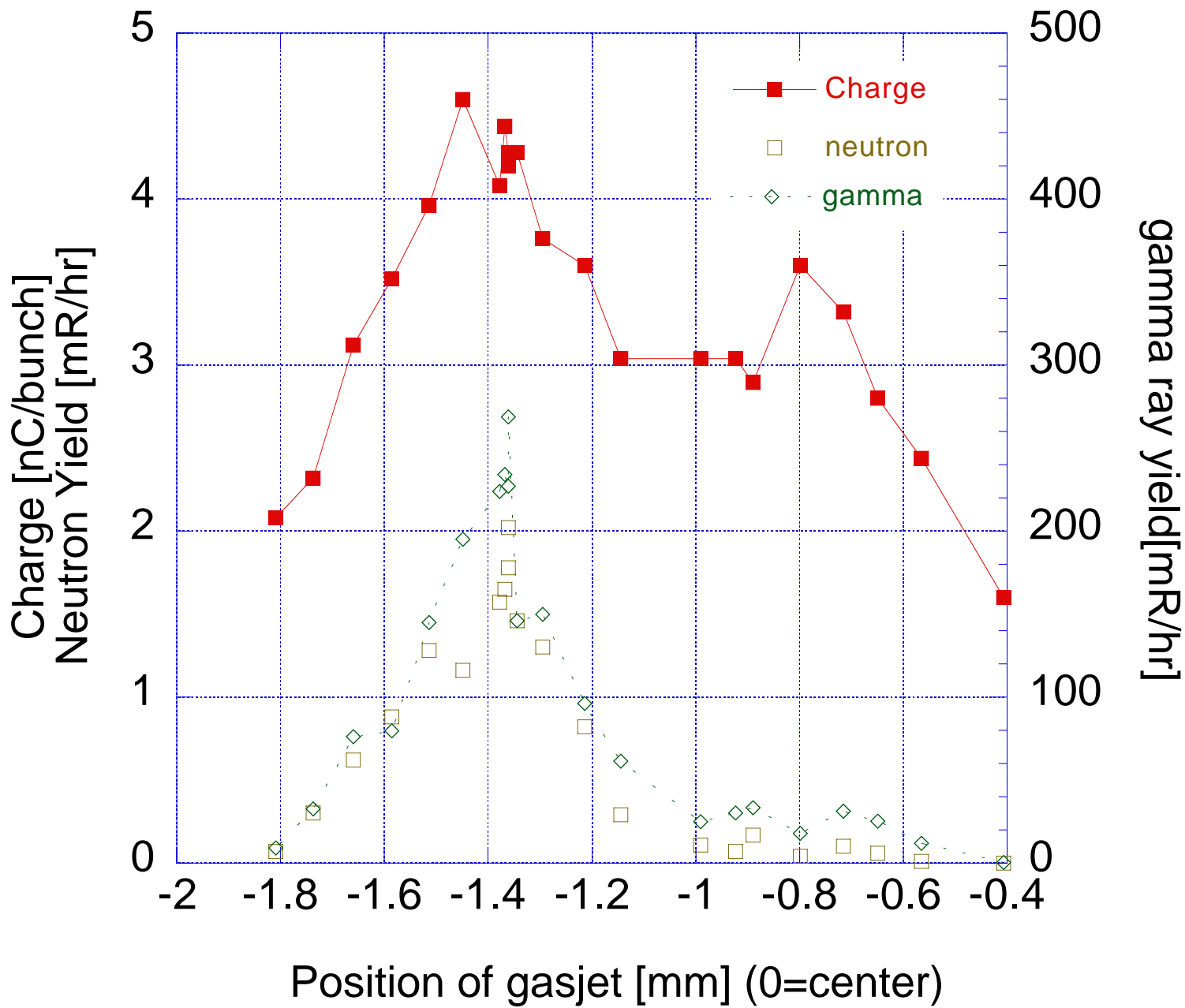


FIG. 4.



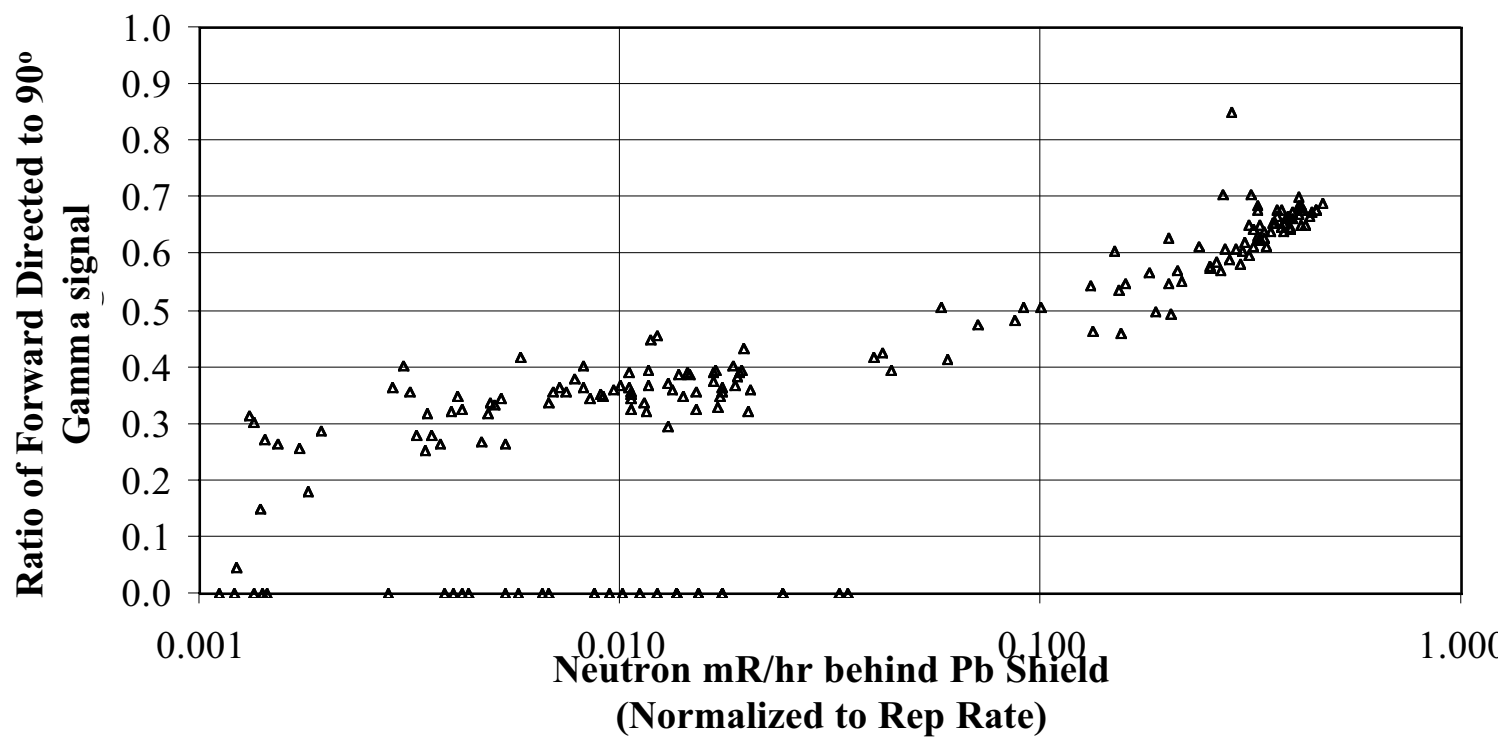


FIG. 5.

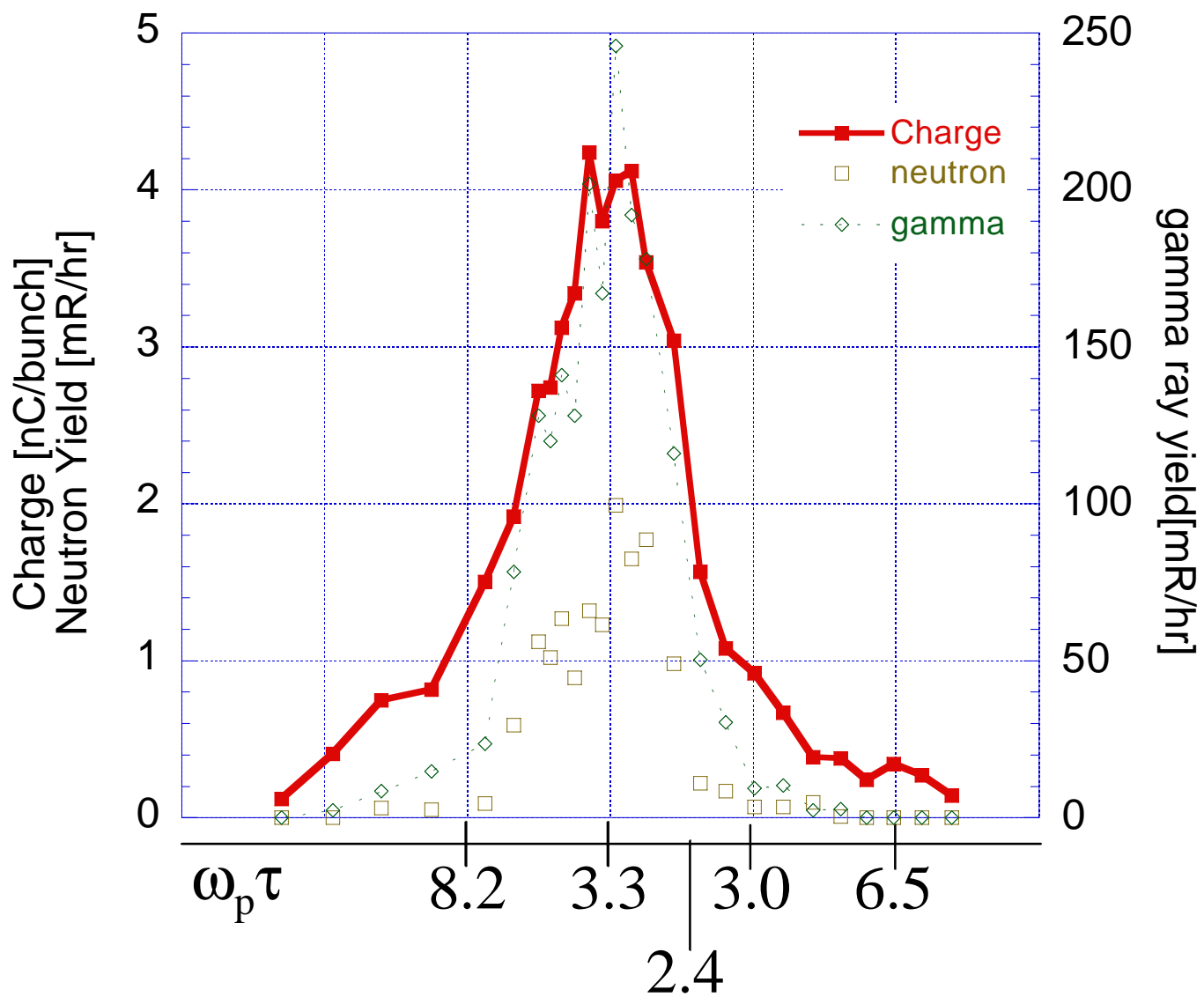


FIG. 6.

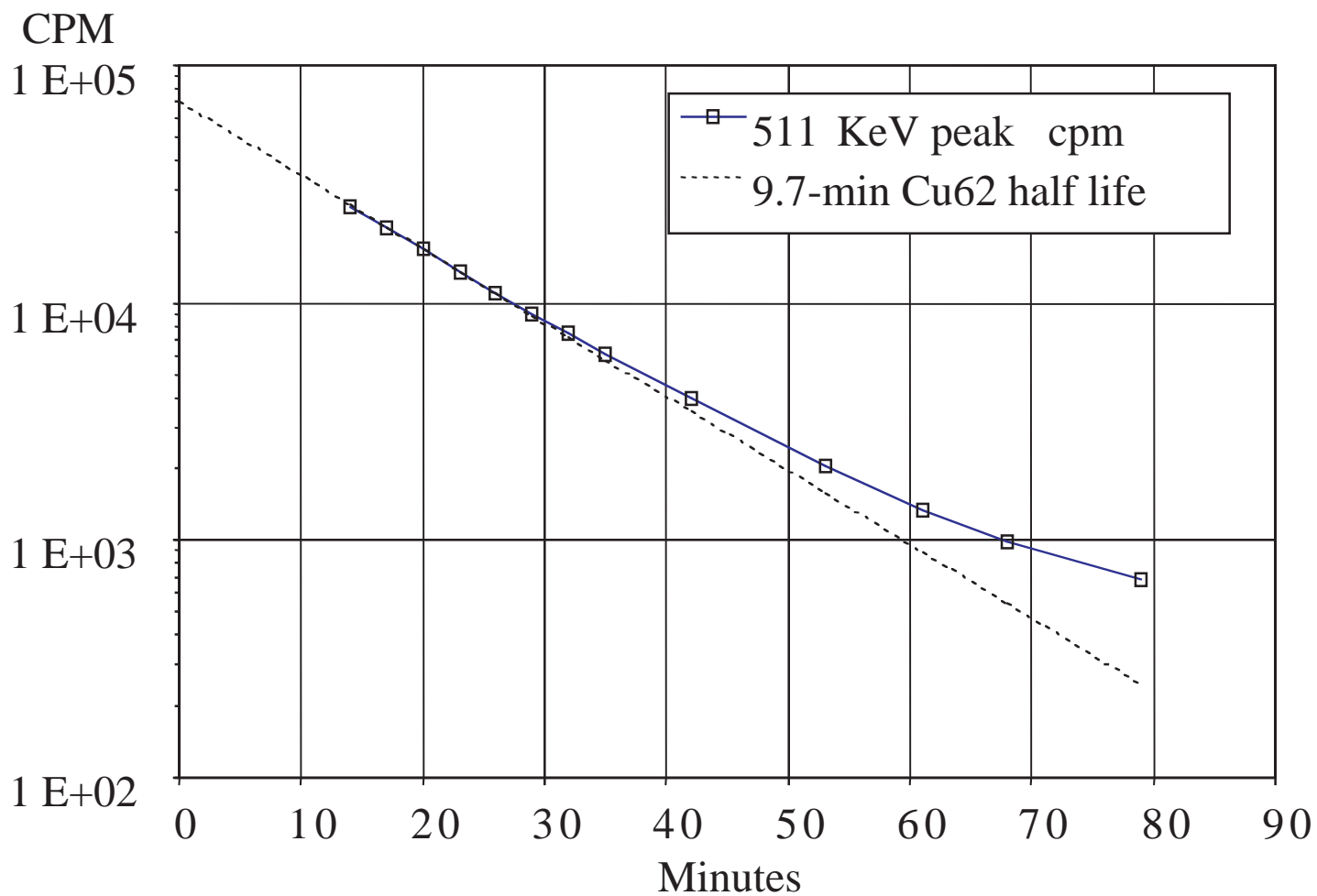


FIG. 7.

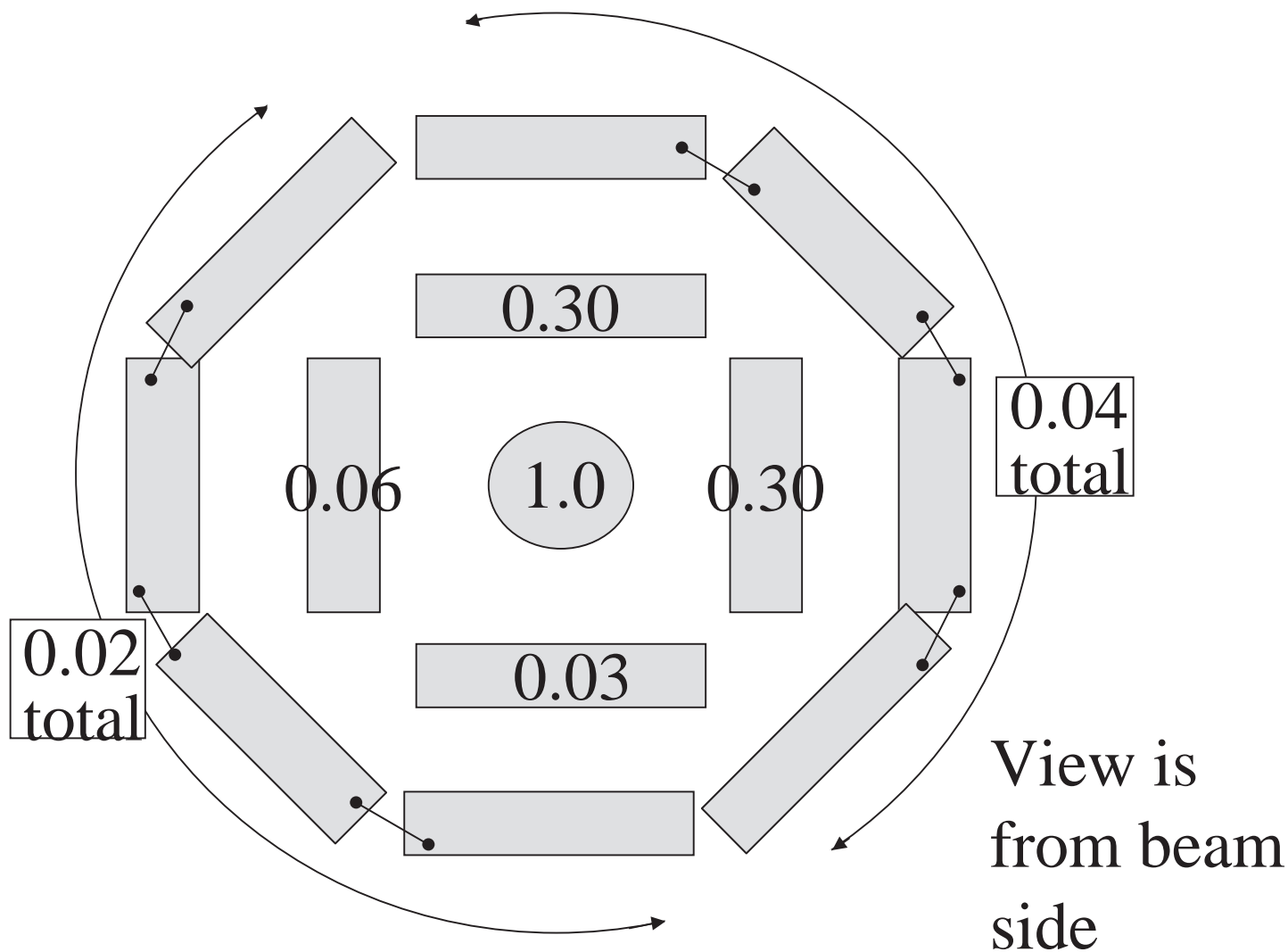


FIG. 8.